Title

Spectroscopic Determination of Key Energy Scales for the Base Hamiltonian of Chromium Trihalides

Journal

The Journal of Physical Chemistry Letters, 12(1)

ISSN

1948-7185

Authors

Shao, YC

Karki, B

Huang, W

et al.

Publication Date

2021-01-14

DOI

10.1021/acs.jpclett.0c03476

Peer reviewed

THE JOURNAL OF PHYSICAL CHEMISTRY LETTERS
A JOURNAL OF THE AMERICAN CHEMICAL SOCIETY

pubs.acs.org/JPCL

Letter

Spectroscopic Determination of Key Energy Scales for the Base Hamiltonian of Chromium Trihalides

Y. C. Shao,* B. Karki, W. Huang, X. Feng, G. Sumanasekera, J.-H. Guo, Y.-D. Chuang,* and B. Freelon*

Cite This: *J. Phys. Chem. Lett.* 2021, 12, 724−731

Read Online

ACCESS | Metrics & More | Article Recommendations | Supporting Information

ABSTRACT: The van der Waals (vdW) chromium trihalides (CrX_3) exhibit field-tunable, two-dimensional magnetic orders that vary with the halogen species and the number of layers. Their magnetic ground states with proximity in energies are sensitive to the degree of ligand−metal (p−d) hybridization and relevant modulations in the Cr d-orbital interactions. We use soft X-ray absorption (XAS) and resonant inelastic X-ray scattering (RIXS) spectroscopy at Cr *L*-edge along with the atomic multiplet simulations to determine the key energy scales such as the crystal field 10 *Dq* and interorbital Coulomb interactions under different ligand metal charge transfer (LMCT) in CrX_3 (X= Cl, Br, and I). Through this systematic study, we show that our approach compared to the literature has yielded a set of more reliably determined parameters for establishing a base Hamiltonian for CrX_3.

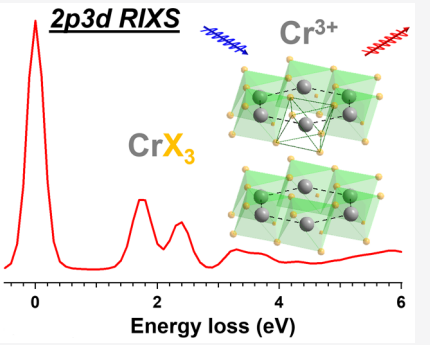

Two-dimensional (2D) materials with unique electronic structures that can host novel magnetic, photonic, electric, and superconducting properties have recently attracted attention because of their potential applications in spintronics, quantum computing, quantum information, catalysts, and energy storage.[1−11] Among these 2D materials, the van der Waals (vdW) semiconductors CrX_3 (X = Cl, Br, and I)[12−15] with hexagonal stacking order and strong spin−lattice interaction have demonstrated highly tunable, layer-dependent magnetic ground states that can be controlled by applied electric field, magnetic field, pressure, and strain.[16−27] This tunability stems from the nearly degenerate ground-state ferromagnetic (FM) and antiferromagnetic (AFM) orders caused by the substitution of halogens that introduces distinct ligand effects on the transition metal (TM) site and modulates the key energy scales such as the crystal field and interorbital Coulomb interaction.[15,28−30] As a result, CrI_3 and $CrCl_3$ can exhibit interlayer FM and AFM couplings, respectively, and even their room-temperature paramagnetic spin moment can be altered by halogen substitution.[31,32] Besides the potential applications, the intricate spin interactions in the projected hexagonal stacking in CrX_3 may manifest phenomena like edge-sharing honeycomb Kitaev physics,[33] spin current,[34] and topological spin excitation that are of great physics interest.[35−37]

To date, density functional theory (DFT) and cluster-based calculations have been used to explain the effects of ligands on the low-temperature magnetic orders in CrX_3 and understand their evolution under the applied electric field;[25−27,29,38] however, energetic proximity between different magnetic ground states sets a stringent requirement for the precision of key energy scales used in the Hamiltonian in these calculations. For example, the magnetic exchange energy in CrX_3 calculated by DFT remains debated as an outcome of imprecision of key energy scales.[39] These theoretical energy scales are often compared with the d−d (for TM complexes; transition between the Cr 3d orbitals) and charge-transfer excitations seen in optical conductivity and Raman spectroscopy, the tabletop techniques with high energy resolution and versatile control of photon polarization for resolving the symmetry of excitations, to gauge their magnitude.[40,41] However, optical conductivity is sensitive to optically allowed transitions (hence suppressed d−d excitations), whereas Raman spectroscopy lacks the elemental, bonding, and orbital sensitivity.[42] On the other hand, soft X-ray spectroscopies such as X-ray absorption (XAS) and, in particular, resonant inelastic X-ray scattering (RIXS) can provide this critical information.[43−46] In this Letter, we report the XAS and RIXS measurements on CrX_3 assisted by the atomic multiplet simulations to extract the key energy scales with varying degrees of ligand−metal charge-transfer (LMCT) effect. We further compare the obtained parameters with the literature to highlight the advantage of using RIXS spectra to better determine their magnitudes.[15,29,38,43,47]

CrX_3 consists of vdW-coupled layers with each layer formed by tilted octahedra where the central Cr^{3+} ion is coordinated with six X-ions. The edge-sharing of octahedra produces a

Received: November 22, 2020
Accepted: December 28, 2020
Published: January 5, 2021

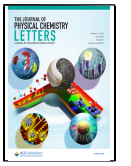

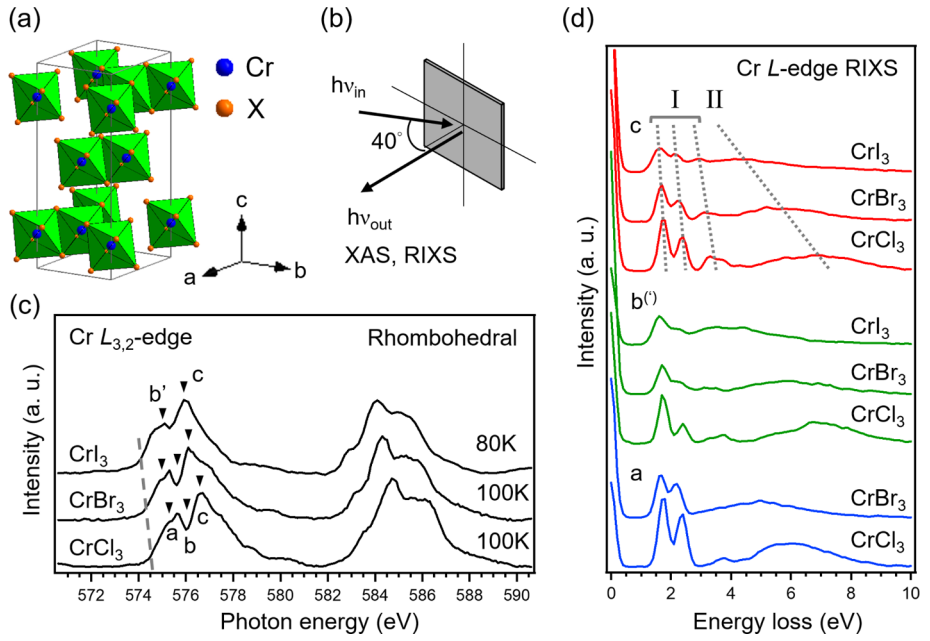

Figure 1. (a) Rhombohedral structure of CrX_3. (b) Schematic plot of the experimental setup. (c) X-ray absorption spectra at Cr $L_{3,2}$-edge of $CrCl_3$, $CrBr_3$, and CrI_3 in the rhombohedral structure phase. The photon energies labeled a, b or b′, and c (inverted triangles) are the excitation energies used in the RIXS measurements. (d) RIXS spectra recorded at excitation photon energies labeled a (blue solid line), b or b′ (green solid line), and c (red solid line) in panel c. The peaks in region I are the d−d excitations, and the broad feature in region II is the charge-transfer excitation.

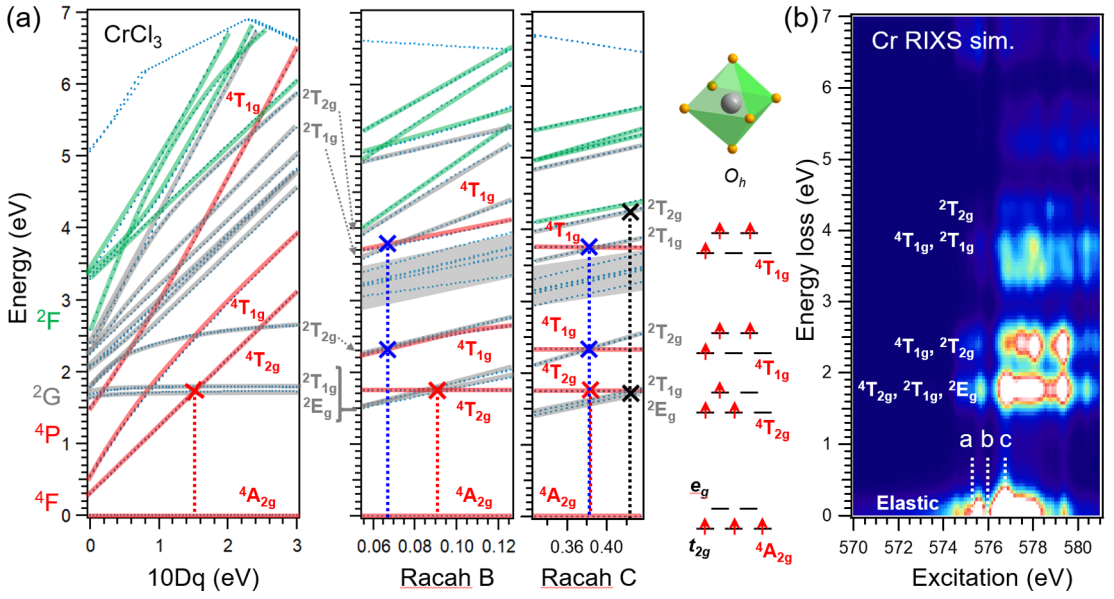

Figure 2. (a) Energy level diagrams of Cr^{3+} in $CrCl_3$ with O_h symmetry for determining the values of the crystal field 10 *Dq* (left), Racah *B* (middle), and Racah *C* (right). The red and gray/green lines are for the quartet and doublet in the $3d^3$ states, respectively. (b) The simulated RIXS spectra as a function of excitation photon energy (RIXS map). The white lines a, b, and c denote the excitation photon energies for the simulated RIXS spectra in Figure 3a. The schematic presentation of the O_h symmetry and the spin/orbital configurations of ^4F ground state, inter-^4F transitions, and ^4F to ^4P transition are shown next to the Racah *C* panel.

honeycomb structure as illustrated in Figure 1a.[31,32] There is a structural phase transition from high-temperature monoclinic to low-temperature rhombohedral phase in bulk $CrCl_3$, $CrBr_3$, and CrI_3 at 240, 420, and 200 K, respectively.[13,31] The magnetic orders emerge at even lower temperatures in the rhombohedral phase;[48−51] therefore, we focus our XAS and RIXS measurements in this phase. The experimental setup is shown in Figure 1b, and the details are described in Experimental and Simulated Methods. The Cr $L_{3,2}$-edge XAS spectra recorded at 100 K for $CrCl_3$ and $CrBr_3$ and at 80 K for CrI_3 are shown in Figure 1c. With halogen substitution from Cl to Br and I, the spectra exhibit a monotonic shift toward lower energy, signaling the weakened ionicity and the stronger influence on the Cr^{3+} site from ligands. This trend is observed in both rhombohedral and monoclinic phases (see Figure S1). In addition to the energy shift, there are subtle changes in the spectral line shape; for example, the features at the L_3 edge are better resolved in $CrCl_3$ (a clear dip at ∼576 eV) than in $CrBr_3$

https://doi.org/10.1021/acs.jpclett.0c03476
J. Phys. Chem. Lett. 2021, 12, 724−731

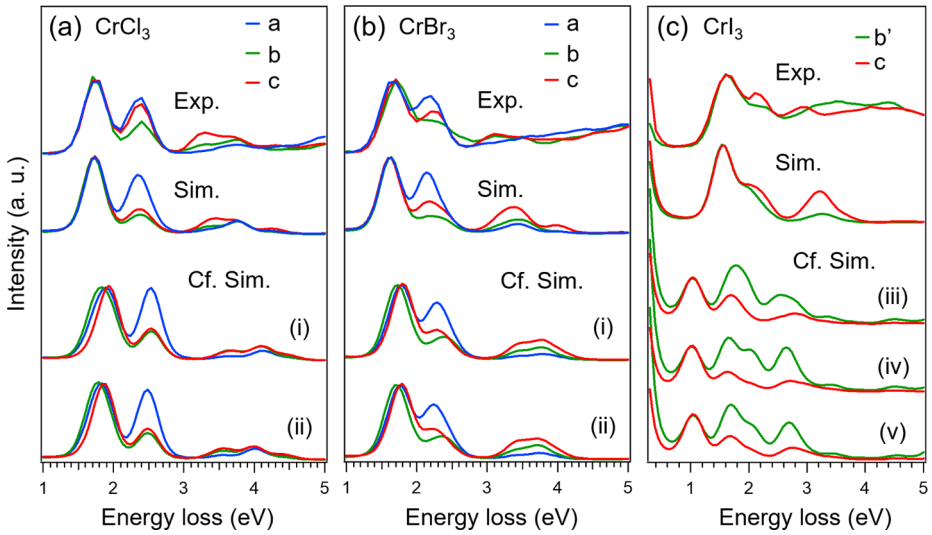

Figure 3. Comparison of experimental (top) and simulated (middle) RIXS spectra of (a) $CrCl_3$, (b) $CrBr_3$, and (c) CrI_3 with parameters determined from ELDs. The compared simulations i−v (bottom) in panels a−c are from the literature.[38,41,47]

and CrI_3, and the high-energy shoulders at $L_{3,2}$ edges are more pronounced in $CrCl_3$.

Although key energy scales such as crystal field, charge transfer, interorbital Coulomb interaction, *etc.* may be extracted by comparing the experimental XAS spectra with the cluster-based calculations, the spectral broadening from finite core-hole lifetime and the contribution of nonlocal excitations above the absorption edge can complicate this approach (see later discussion).[52] On the other hand, it has been suggested that RIXS can provide further information to circumvent these difficulties.[42,43] In Figure 1d, we show the RIXS spectra of CrX_3 recorded at selected excitation photon energies labeled a, b/b′, and c in Figure 1c. The excitation energy a = 575.1 and 575.4 eV for $CrBr_3$ and $CrCl_3$; b' = 575.1 eV for CrI_3, b = 575.6 and 576 eV for $CrBr_3$ and $CrCl_3$; and c = 576, 576.1, and 576.6 eV for CrI_3, $CrBr_3$, and $CrCl_3$, respectively. In these spectra, low-energy excitations around 2 eV energy loss (region I) can be attributed to the inter-Cr 3d orbital transitions (d−d excitations), whereas the broad feature at higher energy loss (region II) is the ligand−metal charge-transfer (LMCT) excitation.[42] Consistent with the XAS spectra, the monotonic energy shift toward smaller energy loss is present in these excitations. Furthermore, this energy shift behavior is also in agreement with Raman spectroscopy.[42]

Unlike XAS and Raman, the well-resolved d−d and LMCT excitations in RIXS spectra offer the opportunity to determine the key energy scales of CrX_3 more reliably. To proceed, we resort to the energy-level diagrams (ELDs) in the atomic multiplet simulations with Cr^{3+} ($3d^3$) state in the O_h symmetry.[43,53] We first choose $CrCl_3$ because of the reduced overlap between its LMCT and d−d excitations. We note that the energy scales of LMCT and crystal field 10 Dq will both affect the energy of $^4A_{2g} \rightarrow {}^4T_{2g}$ excitation in the $3d^3$ system (see Figure S2); to be consistent with the Nephelauxetic effect and DFT calculations,[29,30] we set the LMCT parameters based on the values in the literature.[54,55] The LMCT parameters are listed in Table S1. We also choose the following Racah parameters (the interorbital Coulomb interactions) as a starting point: 0.091 eV, 0.381 eV, and 4.187 for Racah B, Racah C, and C/B, respectively.[29,38] The ELD with varying 10 Dq value using the initial LMCT and Racah parameters is shown in Figure 2a (left panel). In this figure, the term symbols and further substates are assigned by comparing the ELD with the $3d^3$ reference system (see Figure S2 for the determination of term symbol in ELD with different LMCT and Coulomb parameters; see Figure S3 for the discussion about states in the ^2G term symbol).[56] Although the LMCT effect might affect the term symbol and its further substates symbol, this assignment is still useful for the CrX_3 system.[41] The 10 Dq value for $CrCl_3$ is chosen to be 1.55 eV (red dashed line) such that the energy of $^4A_{2g} \rightarrow {}^4T_{2g}$ transition (red cross) matches the first inelastic peak around 1.7 eV energy loss in Figure 1d.

With this 10 Dq value, we fine-tuned the Racah B (middle panel, Racah C is fixed at the initial value of 0.381 eV) and Racah C (right panel, the Racah B is fixed at the new value of 0.067 eV, see later discussion) values using the ELDs, and the results are shown in Figure 2a. From these figures, one can see that the energies of quartet (red lines) and doublet (gray and green lines) states exhibit much stronger dependences on the magnitude of 10 Dq than the Racah B and Racah C, justifying the choice of fixing the 10 Dq value first. For determining the Racah B (blue dashed line and crosses) and Racah C (black dashed line and cross), the term symbols $^4T_{1g}$ (^4F, ∼2.3 eV), $^4T_{1g}$ (^4P, ∼3.8 eV), and $^2T_{2g}$ (^2G, ∼4.2 eV) are used to compare with the energy loss features in the $CrCl_3$ RIXS spectra. In addition, the two doublet states ^2E_g (^2G) and $^2T_{1g}$ (^2G) around 1.7 eV will split away from the $^4T_{2g}$ quartet state if the Racah C value is too small, and this splitting will produce a shoulder on the lower energy loss side. With these considerations, we have determined Racah B and Racah C to be 0.067 and 0.421 eV, respectively, for the presented $CrCl_3$ RIXS spectra. Using these energy scales, we have simulated the excitation photon energy-dependent RIXS spectra (RIXS map) in Figure 2b. The spectra selected at energies marked by a, b, and c (white dashed lines) are shown in Figure 3.

In Figure 3, we show the comparison of experimental (top) and simulated (middle) RIXS spectra at the same excitation photon energies for $CrCl_3$, $CrBr_3$, and CrI_3 in panels (a), (b), and (c), respectively. For $CrBr_3$ and CrI_3, we follow the same approach of using the ELDs and experimental RIXS spectra to determine the energy scales, see Figure S3 for details. For the

https://doi.org/10.1021/acs.jpclett.0c03476
J. Phys. Chem. Lett. 2021, 12, 724−731

Table 1. Electronic Structure Parameters of Cr^{3+} Used in the Atomic Multiplet Simulations[a]

	F^2_{dd} (eV) HF%[c]	F^4_{dd} (eV) HF%[c]	B[b] (eV)	C[b] (eV)	C/B[b]	F^4/F^2	F^2_{pd} (eV) HF%[c]	G^1_{pd} (eV) HF%[c]	G^3_{pd} (eV) HF%[c]	ζ_{2p} (eV) HF%[c]	ζ_{3d} (eV) HF%[c]	10Dq (eV)
$CrCl_3$ $(3d^3)^d$	6.251 58%	5.303 78.5%	0.067	0.421	6.242	0.848	-	-	-	-	0.018 50%	1.55
$CrCl_3$ $(2p^53d^4)^e$	6.726 58%	5.708 78.5%	0.073	0.453	6.242	0.848	5.873 90%	3.828 80%	2.721 100%	5.668 100%	0.024 50%	1.55
$CrBr_3$ $(3d^3)^d$	5.981 55.5%	5.303 78.5%	0.062	0.421	6.797	0.887	-	-	-	-	0.018 50%	1.45
$CrBr_3$ $(2p^53d^4)^e$	6.436 55.5%	5.708 78.5%	0.067	0.453	6.797	0.887	4.894 75%	3.110 65%	2.449 90%	5.668 100%	0.024 50%	1.45
CrI_3 $(3d^3)^d$	5.227 48.5%	5.303 78.5%	0.047	0.421	9.010	1.015	-	-	-	-	0.018 50%	1.45
CrI_3 $(2p^53d^4)^e$	5.624 48.5%	5.708 78.5%	0.050	0.453	9.010	1.015	4.241 65%	2.632 55%	2.177 80%	5.668 100%	0.024 50%	1.45

[a]LMCT and U_{dd} parameters are from reference.[55] U_{dd}/U_{pd} is fixed at 1.25 for all simulations. [b]Racah B, Racah C, and their ratio C/B are rounded to the third decimal place. C/B ratio is calculated using the unrounded values. [c]The percentage shows the scaling factor relative to the atomic Hartree−Fock integrals. [d]Cr^{3+} ground-state parameters (unshaded). [e]Excited-state parameters (shaded) with a 2p core-hole. ζ_{2p} and ζ_{3d} are spin−orbit coupling (SOC) for Cr 2p and 3d orbitals, respectively.

ease of comparison, the intensity of first peak is scaled to be the same in these spectra. From this figure, one can see that the agreement between experiment and simulation is very satisfactory, although certain discrepancies seen in the features at higher energy loss and around 1.4 eV for the low-energy doublet states ^2E_g and $^2T_{1g}$ (^2G) increase from Br to I. These discrepancies can be related to the enhanced interference between the LMCT excitations in the RIXS spectra and the reduced ionicity in CrI_3, and resolving them calls for more precise determination of these parameters (see later discussion).

To demonstrate the advantage of using the experimental RIXS spectra as the starting point for determining the energy scales, we also simulate the CrX_3 RIXS spectra with the parameters from literature (ref 41 and 47 for $CrCl_3$ and $CrBr_3$ and ref 38 for CrI_3; the LMCT parameters of $CrCl_3$ and $CrBr_3$ are taken from ref 55). The resulting simulated spectra (Cf. sim) are shown in the bottom panel of Figure 3. Although the Cf. simulated spectra for $CrCl_3$ and $CrBr_3$ in Figure 3a,b can reproduce the low-energy d−d excitations around 2 eV energy loss, there is a discernible energy shift toward higher energy loss. This energy shift can be attributed to the slightly larger 10 Dq from optical measurements. Moreover, the larger 10 Dq and dissimilar Coulomb parameters also yield different energies for quartet ($^4T_{2g}$) and doublet states (^2E_g and $^2T_{1g}$) such that their varying intensities with respect to the excitation photon energies manifest the seeming shift in the broad feature around 1.7 eV energy loss.

For CrI_3 (Figure 3c), the Racah B, Racah C, and ligand 10 Dq (10 DqL) parameters are not listed in the literature (the 10 DqL values for $CrCl_3$ and $CrBr_3$ are taken from refs 53 and 54 and are listed in Table S1). We resort to the ELDs to find the best values for them, see Figure S4. We have chosen different sets of parameters for Racah B, Racah C, and 10 DqL: 0.122, 0.375, and 0.320 eV for iii; 0.115, 0.429, and 0 eV for iv; and 0.115, 0.429, and 0.320 eV for v. Irrespective to the choices of these parameters, the simulated RIXS spectra are grossly misaligned with the first prominent feature showing up around 1 eV energy loss. This misalignment is due to a much smaller 10 Dq value reported in the literature and is insensitive to the values of other parameters.

We note that the magnetic order does not affect the experimental RIXS spectra (see Figure S5) as the energy scale of magnetic exchange interaction is much smaller than the experimental resolution. Even the variation in the U_{dd} value and 2p3d core-hole effects influence only the intensity of inelastic features in the RIXS spectra, but not their energy positions (see Figure S6 for the details). Furthermore, we simulate the CrX_3 XAS spectra using the energy scales derived from both RIXS (Table 1) and optical measurements in Figure S7, and all simulations can faithfully reproduce the experimental XAS spectra. This exercise further demonstrates that using RIXS instead of XAS can better determine these energy scales.

The energy scales of CrX_3 from this study are summarized in Table 1. Here we focus on the energy scales from RIXS for 3d−3d interaction. In this table, one can see that the magnitude of crystal field 10 Dq decreases from Cl to Br and I, which can be understood from the spectrochemical series for the strength of various ligand-induced crystal field: I^- < Br^- < Cl^-.[30] The interorbital Coulomb interactions, as defined by the Racah parameters in metal complexes, generally vary as the ligand changes. As suggested by the Nephelauxetic effect (series), the most ionic (covalent) bond should lead to a

https://doi.org/10.1021/acs.jpclett.0c03476
J. Phys. Chem. Lett. 2021, 12, 724−731

smaller (larger) reduction in the Racah parameters relative to the atomic values.[30] Per the electronegativities, the degree of ionicity should decrease from $CrCl_3$ to $CrBr_3$ to CrI_3, and our reported Racah B values display this expected trend. The values of Racah B and Racah C, related to the Coulomb Slater integrals F^2_{dd} and F^4_{dd}, respectively (see the Experimental and Simulated Methods), do not always yield a fixed ratio.[30] Because Racah C value is constant and Racah B value increases with ionicity, the ratio C/B will increase from the ionic bonding ($CrCl_3$) to the covalent bonding (CrI_3) and exceed the standard value (3.75−4).[43] It is noted that the ratio F^4_{dd}/F^2_{dd} can become larger than the standard value (∼0.63) if the d−p screening effect is considered.[57,58] This screening effect is treated in the DFT calculations for CrX_3,[29] and the reported reduced trend from calculation is also seen in Table 1.

It has been shown that the spin moment of Cr is larger than the nominal $3\mu_B$/Cr value in both $CrCl_3$ and CrI_3.[31,32] The larger spin moment can be understood from the LMCT effect that the Cr 3d orbital occupation is more than $3d^3$ (see Table S2). Using the 10 Dq values and the Hund's rule exchange $J_H = \frac{F^2_{dd} + F^4_{dd}}{14}$[29,54,57] to analyze the high spin state,[59] we obtained the J_H values of 0.825 and 0.752 eV for $CrCl_3$ and CrI_3, respectively. These J_H values are similar to those reported in the literature.[29] Because the 10 Dq values are smaller than two times the J_H values, this implies that both $CrCl_3$ and CrI_3 will prefer the high spin, i.e., more e_g spin-up occupations from LMCT electrons than t_{2g} spin-down ones (see Table S2), and justifies the aforementioned analysis.

In conclusion, we present the XAS and RIXS measurements on CrX_3. Using the ELDs in atomic multiplet calculations with the consideration of LMCT effect, we can reliably extract energy scales as summarized in Table 1. These parameters, compared to the literature values that were derived from optical and XAS spectra, can well-produce the experimental RIXS spectra. This substantiates the claim that starting with the RIXS spectra is a much more accurate approach to obtain these energy scales than XAS despite its relatively lower energy resolution. One can envision that higher energy resolution RIXS spectroscopy will be beneficial for extending the current work to explore the temperature dependence of these energy scales when CrX_3 is driven to different magnetic ground states.

EXPERIMENTAL AND SIMULATED METHODS

CrX_3 Crystal Growth. Single-crystal $CrBr_3$ samples were produced by a short chemical vapor transport (CVT) method where an evacuated quartz tube loaded with the mixture of chromium (Cr, Alfa Aesar 99%) and tellurium bromide ($TeBr_4$, Alfa Aesar 99.9%) powders was annealed at a temperature gradient of 750/450 °C for 72 h. The single-crystal $CrCl_3$ samples were synthesized by vacuum sublimation of commercially available $CrCl_3$ powder (Alfa Aesar 99.9%) at a temperature gradient of 700/550 °C for 72 h. Ampule with precursors was evacuated down to 10^{-6} Torr and sealed afterward using an oxy-acetylene flame torch. Sealed tubes are placed in a three-zone furnace (MTI OTF-1200X) for annealing in such a way that the hot end of the tube was placed toward the center of the furnace. The evacuated ampule with samples were heated at 3 °C/min to 700−750 °C, annealed for 72 h, and cooled to room temperature at 5 °C/min. Several thin flakes of $CrBr_3$ and $CrCl_3$ single crystals were formed at the cold end of the quartz tube.[60] CrI_3 single crystals were purchased from HQ Graphene (Groningen, The Netherlands).

XAS and RIXS Measurement. The XAS (total fluorescence yield mode, TFY) and RIXS measurements were performed in the qRIXS endstation at Beamline 8.0.1 at the Advanced Light Source (ALS), Lawrence Berkeley National Laboratory (LBNL).[61] The air- and light-sensitive CrI_3 samples were cleaved *ex situ* in a dark Ar environment before being introduced into the experimental chamber. For $CrCl_3$ and $CrBr_3$ crystals, they were loaded into the experimental chamber right out of the sealed quartz tubes without cleavage. The experimental chamber was maintained at dark conditions and high vacuum (5×10^{-9} Torr) during the measurements. The X-ray photon polarization was kept in the horizontal scattering plane (π-polarization), and the combined (beamline and spectrometer) energy resolution was 0.3 eV (0.35 eV) for $CrCl_3$ and $CrBr_3$ (CrI_3) at Cr L-edge. An open cycle cryostat with liquid nitrogen (LN_2) flow was used to cool the CrX_3 samples to 80 K or 100 K for the measurements in the rhombohedral structural phase. The angle between the incident X-ray beam and the photon detector (a GaAsP photodiode with a front aluminum window to block out the visible light and photoelectrons, for TFY mode of XAS) and X-ray spectrometer (for RIXS,[62]) was 40°, and the sample normal was pointing to the detector/spectrometer (see the experimental schematic in Figure 1b). The sample orientations were not aligned for specific order states. The XAS spectra were first normalized by the photocurrent from an upstream Au mesh; the pre- and postedge spectral weights were then set to zero. We used the elastic peak from a carbon tape to convert the pixel number of the 2D CCD detector on the spectrometer to the emission energy in electronvolts. For RIXS spectra in Figure 1d, the collection time of each spectrum was fixed and the intensity was normalized by total counts on the CCD detector.

Energy-Level Diagrams and RIXS Simulation. The quantum many-body script language QUANTY and CRISPY, implemented in QUANTY, were used to calculate the ELDs and simulate the RIXS and XAS spectra.[54,63−65] The ELDs were scanned to capture the energy level of all Cr^{3+} ($3d^3$) subconfigurations in various crystal fields and $3d^3$ electron Coulomb interactions. In the present work, we use the single Cr site atomic multiplet calculations and consider the effect from ligands through LMCT. The crystal field 10 Dq, 3d Coulomb interactions, 3d spin−orbital coupling, and the LMCT are taken into account for the Hamiltonian of the ELDs; moreover, the configurations of $3d^3$ and $3d^4$ were taken into account because of the LMCT effect. The Racah parameters comprising Coulomb Slater integrals F^k_{dd} (k = 0, 2, 4 for 3d system) were used to describe the intra-atomic 3d3d multipole Coulomb interaction in the system. The definitions of two major Racah parameters for intra-atomic 3d3d multipole interaction, Racah B and Racah C, are $B = \frac{9 \times F^2_{dd} - 5 \times F^4_{dd}}{441}$ and $C = \frac{5 \times F^4_{dd}}{63}$. We do not discuss the Racah $A = F^0_{dd} - \frac{F^4_{dd}}{9}$ on all 3d subconfigurations because it only introduces a constant offset to the spectra. The average on-site Coulomb repulsion between two d-orbitals is $U_{dd} = F^0_{dd} - \frac{2}{63}(F^2_{dd} + F^4_{dd})$. On the other hand, the Coulomb Slater integrals F^k_{pd} (k = 0, 2 for the 2p3d system) and exchange Slater integrals G^k_{pd} (k = 1, 3 for the 2p3d system) are considered for the core−valence interaction. The Coulomb

https://doi.org/10.1021/acs.jpclett.0c03476
J. Phys. Chem. Lett. 2021, 12, 724−731

interaction between the 2p-core hole and 3d electrons is $U_{pd} = F^0_{pd} - \frac{1}{15}G^1_{pd} - \frac{3}{70}G^3_{pd}$. All Slater integrals, U_{dd}, and U_{pd} mentioned above are included as a part of the Hamiltonian for the XAS and RIXS simulations by using CRISPY. To compare the simulated RIXS spectra with the experimental spectra, the Gaussian broadening of 0.35 eV for CrI_3 and 0.3 eV for $CrCl_3$ and $CrBr_3$ was applied to the simulated spectra.

■ ASSOCIATED CONTENT

Supporting Information

The Supporting Information is available free of charge at https://pubs.acs.org/doi/10.1021/acs.jpclett.0c03476.

XAS of chromium trihalides at room temperature; ELDs with different LMCT and Coulomb parameters; ELDs for the key energy scales of $CrBr_3$ and CrI_3; ELDs for estimating the Racah *B*, Racah *C*, and ligand 10*Dq* of CrI_3 for the simulation using parameters in the literature (compared spectra in the main text); experimental RIXS at low temperature; U and 2p−3d interaction in RIXS simulation; XAS simulations based on the key energy scales from simulated and experimental RIXS (PDF)

■ AUTHOR INFORMATION

Corresponding Authors

Y. C. Shao − *Advanced Light Source, Lawrence Berkeley National Laboratory, Berkeley, California 94720, United States; Department of Physics, University of Houston, Houston, Texas 77204, United States;* orcid.org/0000-0002-6691-3799; Email: yshao@lbl.gov

Y.-D. Chuang − *Advanced Light Source, Lawrence Berkeley National Laboratory, Berkeley, California 94720, United States;* orcid.org/0000-0002-2773-3840; Email: ychuang@lbl.gov

B. Freelon − *Department of Physics and Texas Center for Superconductivity, University of Houston, Houston, Texas 77204, United States*; Email: bkfreelon@uh.edu

Authors

B. Karki − *Department of Physics and Astronomy, University of Louisville, Louisville, Kentucky 40292, United States;* orcid.org/0000-0002-9942-2056

W. Huang − *Advanced Light Source, Lawrence Berkeley National Laboratory, Berkeley, California 94720, United States; State Key Laboratory of Functional Materials for Informatics, Shanghai Institute of Microsystem and InformationTechnology, Chinese Academy of Sciences, Shanghai 200050, China*

X. Feng − *Advanced Light Source, Lawrence Berkeley National Laboratory, Berkeley, California 94720, United States*

G. Sumanasekera − *Department of Physics and Astronomy, University of Louisville, Louisville, Kentucky 40292, United States*

J.-H. Guo − *Advanced Light Source, Lawrence Berkeley National Laboratory, Berkeley, California 94720, United States;* orcid.org/0000-0002-8576-2172

Complete contact information is available at: https://pubs.acs.org/10.1021/acs.jpclett.0c03476

Notes

The authors declare no competing financial interest.

■ ACKNOWLEDGMENTS

We thank Y. Lu for valuable discussions of the theoretical simulation. This research used resources of the Advanced Light Source (ALS), a U.S. DOE Office of Science User Facility under contract number DE-AC02-05CH11231. Work at University of Houston was supported by the State of Texas through TcSUH.

■ REFERENCES

(1) Schwierz, F. Graphene Transistors. *Nat. Nanotechnol.* **2010**, *5*, 487−496.

(2) Manzeli, S.; Ovchinnikov, D.; Pasquier, D.; Yazyev, O. V.; Kis, A. 2D Transition Metal Dichalcogenides. *Nat. Rev. Mater.* **2017**, *2*, 17033.

(3) Avsar, A.; Ochoa, H.; Guinea, F.; Özyilmaz, B.; Van Wees, B. J.; Vera-Marun, I. J. Colloquium: Spintronics in graphene and other two-dimensional materials. *Rev. Mod. Phys.* **2020**, *92*, 21003.

(4) Liu, C.; Chen, H.; Wang, S.; Liu, Q.; Jiang, Y. G.; Zhang, D. W.; Liu, M.; Zhou, P. Two-dimensional materials for next-generation computing technologies. *Nat. Nanotechnol.* **2020**, *15*, 545−557.

(5) Sangwan, V. K.; Hersam, M. C. Electronic Transport in Two-Dimensional Materials. *Annu. Rev. Phys. Chem.* **2018**, *69*, 299.

(6) Das, S.; Robinson, J. A.; Dubey, M.; Terrones, H.; Terrones, M. Beyond Graphene: Progress in Novel Two-Dimensional Materials and van der Waals Solids. *Annu. Rev. Mater. Res.* **2015**, *45*, 1−27.

(7) Shim, J.; Park, H. Y.; Kang, D. H.; Kim, J. O.; Jo, S. H.; Park, Y.; Park, J. H. Electronic and Optoelectronic Devices based on Two-Dimensional Materials: From Fabrication to Application. *Adv. Electron. Mater.* **2017**, *3*, 1600364.

(8) Zeng, M.; Xiao, Y.; Liu, J.; Yang, K.; Fu, L. Exploring Two-Dimensional Materials toward the Next-Generation Circuits: From Monomer Design to Assembly Control. *Chem. Rev.* **2018**, *118*, 6236−6296.

(9) Chen, S.; Shi, G. Two-Dimensional Materials for Halide Perovskite-Based Optoelectronic Devices. *Adv. Mater.* **2017**, *29*, 1605448.

(10) Lu, X.; Stepanov, P.; Yang, W.; Xie, M.; Aamir, M. A.; Das, I.; Urgell, C.; Watanabe, K.; Taniguchi, T.; Zhang, G.; Bachtold, A.; MacDonald, A. H.; Efetov, D. K. Superconductors, orbital magnets and correlated states in magic-angle bilayer graphene. *Nature* **2019**, *574*, 653−657.

(11) Cao, Y.; Rodan-Legrain, D.; Rubies-Bigorda, O.; Park, J. M.; Watanabe, K.; Taniguchi, T.; Jarillo-Herrero, P. Tunable correlated states and spin-polarized phases in twisted bilayer-bilayer graphene. *Nature* **2020**, *583*, 215.

(12) Handy, L. L.; Gregory, N. W. Structural Properties of Chromium(III) Iodide and Some Chromium(III) Mixed Halides. *J. Am. Chem. Soc.* **1952**, *74*, 891−893.

(13) Morosin, B.; Narath, A. X-Ray Diffraction and Nuclear Quadrupole Resonance Studies of Chromium Trichloride. *J. Chem. Phys.* **1964**, *40*, 1958−1967.

(14) Pollini, I. Electron Correlations and Hybridization in Chromium Compounds. *Solid State Commun.* **1998**, *106*, 549−554.

(15) Wang, H.; Eyert, V.; Schwingenschlögl, U. Electronic Structure and Magnetic Ordering of the Semiconducting Chromium Trihalides $CrCl_3$, $CrBr_3$, and CrI_3. *J. Phys.: Condens. Matter* **2011**, *23*, 116003.

(16) Chen, W.; Sun, Z.; Wang, Z.; Gu, L.; Xu, X.; Wu, S.; Gao, C. Direct Observation of van der Waals Stacking-Dependent Interlayer Magnetism. *Science* **2019**, *366*, 983−987.

(17) Li, T.; Jiang, S.; Sivadas, N.; Wang, Z.; Xu, Y.; Weber, D.; Goldberger, J. E.; Watanabe, K.; Taniguchi, T.; Fennie, C. J.; Fai Mak, K.; Shan, J. Pressure-Controlled Interlayer Magnetism in Atomically Thin CrI_3. *Nat. Mater.* **2019**, *18*, 1303−1308.

(18) Sivadas, N.; Okamoto, S.; Xiao, D. Gate-Controllable Magneto-optic Kerr Effect in Layered Collinear Antiferromagnets. *Phys. Rev. Lett.* **2016**, *117*, 267203.

(19) Huang, B.; Clark, G.; Navarro-Moratalla, E.; Klein, D. R.; Cheng, R.; Seyler, K. L.; Zhong, Di; Schmidgall, E.; McGuire, M. A.;

Cobden, D. H.; Yao, W.; Xiao, D.; Jarillo-Herrero, P.; Xu, X. Layer-dependent ferromagnetism in a van der Waals crystal down to the monolayer limit. *Nature* **2017**, *546*, 270−273.
(20) Jiang, S.; Li, L.; Wang, Z.; Mak, K. F.; Shan, J. Controlling magnetism in 2D CrI_3 by electrostatic doping. *Nat. Nanotechnol.* **2018**, *13*, 549−553.
(21) Gibertini, M.; Koperski, M.; Morpurgo, A. F.; Novoselov, K. S. Magnetic 2D materials and heterostructures. *Nat. Nanotechnol.* **2019**, *14*, 408−419.
(22) Mondal, S.; Kannan, M.; Das, M.; Govindaraj, L.; Singha, R.; Satpati, B.; Arumugam, S.; Mandal, P. Effect of hydrostatic pressure on ferromagnetism in two-dimensional CrI_3. *Phys. Rev. B: Condens. Matter Mater. Phys.* **2019**, *99*, 180407.
(23) Kim, H. H.; Yang, B.; Li, S.; Jiang, S.; Jin, C.; Tao, Z.; Nichols, G.; Sfigakis, F.; Zhong, S.; Li, C.; Tian, S.; Cory, D. G.; Miao, G. X.; Shan, J.; Mak, K. F.; Lei, H.; Sun, K.; Zhao, L.; Tsen, A. W. Evolution of interlayer and intralayer magnetism in three atomically thin chromium trihalides. *Proc. Natl. Acad. Sci. U. S. A.* **2019**, *116*, 11131−11136.
(24) Zhang, Y.; Holder, T.; Ishizuka, H.; de Juan, F.; Nagaosa, N.; Felser, C.; Yan, B. Switchable magnetic bulk photovoltaic effect in the two-dimensional magnet CrI_3. *Nat. Commun.* **2019**, *10*, 3783.
(25) Jiang, S.; Shan, J.; Mak, K. F. Electric-Field Switching of Two-Dimensional van der Waals Magnets. *Nat. Mater.* **2018**, *17*, 406−410.
(26) Wu, Z.; Yu, J.; Yuan, S. Strain-Tunable Magnetic and Electronic Properties of Monolayer CrI_3. *Phys. Chem. Chem. Phys.* **2019**, *21*, 7750−7755.
(27) Xu, R.; Zou, X. Electric Field-Modulated Magnetic Phase Transition in van der Waals CrI_3 Bilayers. *J. Phys. Chem. Lett.* **2020**, *11*, 3152−3158.
(28) Jang, S. W.; Jeong, M. Y.; Yoon, H.; Ryee, S.; Han, M. J. (2019). Microscopic understanding of magnetic interactions in bilayer CrI3. *Phys. Rev. Mater.* **2019**, *3*, 031001.
(29) Besbes, O.; Nikolaev, S.; Meskini, N.; Solovyev, I. Microscopic Origin of Ferromagnetism in the Trihalides $CrCl_3$ and CrI_3. *Phys. Rev. B: Condens. Matter Mater. Phys.* **2019**, *99*, 104432.
(30) Tchougréeff, A. L.; Dronskowski, R. Nephelauxetic Effect Revisited. *Int. J. Quantum Chem.* **2009**, *109*, 2606−2621.
(31) McGuire, M. A.; Dixit, H.; Cooper, V. R.; Sales, B. C. Coupling of Crystal Structure and Magnetism in the Layered, Ferromagnetic Insulator CrI_3. *Chem. Mater.* **2015**, *27*, 612−620.
(32) McGuire, M. A.; Clark, G.; Kc, S.; Chance, W. M.; Jellison, G. E.; Cooper, V. R.; Xu, X.; Sales, B. C. Magnetic Behavior and Spin-Lattice Coupling in Cleavable van der Waals Layered $CrCl_3$ Crystals. *Phys. Rev. Mater.* **2017**, *1*, 014001.
(33) Lee, I.; Utermohlen, F. G.; Weber, D.; Hwang, K.; Zhang, C.; VanTol, J.; Goldberger, J. E.; Trivedi, N.; Hammel, P. C. Fundamental Spin Interactions Underlying the Magnetic Anisotropy in the Kitaev Ferromagnet CrI_3. *Phys. Rev. Lett.* **2020**, *124*, 017201.
(34) Klein, D. R.; MacNeill, D.; Lado, J. L.; Soriano, D.; Navarro-Moratalla, E.; Watanabe, K.; Taniguchi, T.; Manni, S.; Canfield, P.; Fernández-Rossier, J.; Jarillo-Herrero, P. Probing Magnetism in 2D van der Waals Crystalline Insulators via Electron Tunneling. *Science* **2018**, *360*, 1218−1222.
(35) Chen, L.; Chung, J. H.; Gao, B.; Chen, T.; Stone, M. B.; Kolesnikov, A. I.; Huang, Q.; Dai, P. Topological Spin Excitations in Honeycomb Ferromagnet CrI_3. *Phys. Rev. X* **2018**, *8*, 041028.
(36) Baidya, S.; Yu, J.; Kim, C. H. Tunable Magnetic Topological Insulating Phases in Monolayer CrI_3. *Phys. Rev. B: Condens. Matter Mater. Phys.* **2018**, *98*, 155148.
(37) Lado, J. L.; Fernández-Rossier, J. On the Origin of Magnetic Anisotropy in Two Dimensional CrI_3. *2D Mater.* **2017**, *4*, 035002.
(38) Kim, D. H.; Kim, K.; Ko, K. T.; Seo, J.; Kim, J. S.; Jang, T. H.; Kim, Y.; Kim, J. Y.; Cheong, S. W.; Park, J. H. Giant Magnetic Anisotropy Induced by Ligand LS Coupling in Layered Cr Compounds. *Phys. Rev. Lett.* **2019**, *122*, 207201.
(39) Soriano, D.; Katsnelson, M. I.; Fernández-Rossier, J. Magnetic Two-Dimensional Chromium Trihalides: A Theoretical Perspective. *Nano Lett.* **2020**, *20*, 6225−6234.
(40) Shinagawa, K.; Sato, H.; Ross, H. J.; McAven, L. F.; Butler, P. H. Charge-Transfer Transitions in Chromium Trihalides. *J. Phys.: Condens. Matter* **1996**, *8*, 8457−8463.
(41) Dillon, J. F.; Kamimura, H.; Remeika, J. P. Magneto-Optical Properties of Ferromagnetic Chromium Trihalides. *J. Phys. Chem. Solids* **1966**, *27*, 1531−1549.
(42) Seyler, K. L.; Zhong, D.; Klein, D. R.; Gao, S.; Zhang, X.; Huang, B.; Navarro-Moratalla, E.; Yang, L.; Cobden, D. H.; McGuire, M. A.; Yao, W.; Xiao, D.; Jarillo-Herrero, P.; Xu, X. Ligand-Field Helical Luminescence in a 2D Ferromagnetic Insulator. *Nat. Phys.* **2018**, *14*, 277−281.
(43) Hunault, M. O. J. Y.; Harada, Y.; Miyawaki, J.; Wang, J.; Meijerink, A.; DeGroot, F. M. F.; VanSchooneveld, M. M. Direct Observation of Cr^{3+} 3d States in Ruby: Toward Experimental Mechanistic Evidence of Metal Chemistry. *J. Phys. Chem. A* **2018**, *122*, 4399−4413.
(44) Shao, Y. C.; Wray, L. A.; Huang, S. W.; Liu, Y. S.; Song, W.; Yang, S.; Chuang, Y.-D.; Guo, J.; Pong, W. F. The Key Energy Scales of Gd-Based Metallofullerene Determined by Resonant Inelastic X-Ray Scattering Spectroscopy. *Sci. Rep.* **2017**, *7*, 8125.
(45) Frisk, A.; Duffy, L. B.; Zhang, S.; van der Laan, G.; Hesjedal, T. Magnetic X-Ray Spectroscopy of Two-Dimensional CrI_3 Layers. *Mater. Lett.* **2018**, *232*, 5−7.
(46) Ament, L. J. P.; VanVeenendaal, M.; Devereaux, T. P.; Hill, J. P.; Van DenBrink, J. Resonant Inelastic X-Ray Scattering Studies of Elementary Excitations. *Rev. Mod. Phys.* **2011**, *83*, 705−767.
(47) Pedroli, G.; Pollini, I.; Spinolo, G. Specific Magnetic Rotation Spectra and Crystal Field Calculation in $CrBr_3$ and $CrCl_3$. *J. Phys. C: Solid State Phys.* **1975**, *8*, 2317−2322.
(48) de Haas, W. J.; Schultz, B. H.; Koolhaas, M. J. Further measurements of the magnetic Properties of some salts of the iron gpoup at low temperatures. *Physica* **1940**, *7*, 57.
(49) Cable, J. W.; Wilkinson, M. K.; Wollan, E. O. Neutron diffraction investigation of antiferromagnetism in $CrCl_3$. *J. Phys. Chem. Solids* **1961**, *19*, 29−34.
(50) Tsubokawa, I. On the Magnetic Properties of a $CrBr_3$ Single Crystal. *J. Phys. Soc. Jpn.* **1960**, *15*, 1664.
(51) Dillon, J. F.; Olson, C. E. Magnetization, Resonance, and Optical Properties of the Ferromagnet CrI_3. *J. Appl. Phys.* **1965**, *36*, 1259−1260.
(52) Bisogni, V.; Catalano, S.; Green, R. J.; Gibert, M.; Scherwitzl, R.; Huang, Y.; Strocov, V. N.; Zubko, P.; Balandeh, S.; Triscone, J. M.; Sawatzky, G.; Schmitt, T. Ground-state oxygen holes and the metal-insulator transition in the negative charge-transfer rare-earth nickelates. *Nat. Commun.* **2016**, *7*, 13017.
(53) Ghiringhelli, G.; Matsubara, M.; Dallera, C.; Fracassi, F.; Gusmeroli, R.; Piazzalunga, A.; Tagliaferri, A.; Brookes, N. B.; Kotani, A.; Braicovich, L. NiO as a Test Case for High Resolution Resonant Inelastic Soft X-Ray Scattering. *J. Phys.: Condens. Matter* **2005**, *17*, 5397−5412.
(54) Haverkort, M. W.; Zwierzycki, M.; Andersen, O. K. Multiplet Ligand-Field Theory Using Wannier Orbitals. *Phys. Rev. B: Condens. Matter Mater. Phys.* **2012**, *85*, 165113.
(55) Feldkemper, S.; Weber, W. Generalized calculation of magnetic coupling constants for Mott-Hubbard insulators: Application to ferromagnetic Cr compounds. *Phys. Rev. B: Condens. Matter Mater. Phys.* **1998**, *57*, 7755−7766.
(56) *The Integrated Approach to Chemistry Laboratory: Selected Experiments*; Basu, P., Johnson, M., Eds.; DEStech Publications: Lancaster, PA, 2009; pp 74.
(57) Vaugier, L.; Jiang, H.; Biermann, S. Hubbard U and Hund Exchange J in Transition Metal Oxides: Screening versus Localization Trends from Constrained Random Phase Approximation. *Phys. Rev. B: Condens. Matter Mater. Phys.* **2012**, *86*, 165105.
(58) Solovyev, I. V. Combining DFT and Many-Body Methods to Understand Correlated Materials. *J. Phys.: Condens. Matter* **2008**, *20*, 293201.
(59) Tomiyasu, K.; Okamoto, J.; Huang, H. Y.; Chen, Z. Y.; Sinaga, E. P.; Wu, W. B.; Chu, Y. Y.; Singh, A.; Wang, R. P.; De Groot, F. M.

https://doi.org/10.1021/acs.jpclett.0c03476
J. Phys. Chem. Lett. 2021, 12, 724−731

F.; Chainani, A.; Ishihara, S.; Chen, C. T.; Huang, D. J. Coulomb Correlations Intertwined with Spin and Orbital Excitations in $LaCoO_3$. *Phys. Rev. Lett.* **2017**, *119*, 196402.
(60) Abramchuk, M.; Jaszewski, S.; Metz, K. R.; Osterhoudt, G. B.; Wang, Y.; Burch, K. S.; Tafti, F. Controlling Magnetic and Optical Properties of the van der Waals Crystal $CrCl_{3-x}Br_x$ via Mixed Halide Chemistry. *Adv. Mater.* **2018**, *30*, 1801325.
(61) Chuang, Y. D.; Feng, X.; Cruz, A.; Hanzel, K.; Brown, A.; Spucces, A.; Frano, A.; Lee, W. S.; Kim, J.; Chen, Y. J. Momentum-Resolved Resonant Inelastic Soft X-Ray Scattering (QRIXS) Endstation at the ALS. *J. Electron Spectrosc. Relat. Phenom.* **2019**, 146897.
(62) Chuang, Y.-D.; Shao, Y.-C.; Cruz, A.; Hanzel, K.; Brown, A.; Frano, A.; Qiao, R.; Smith, B.; Domning, E.; Huang, S.-W.; et al. Modular Soft X-Ray Spectrometer for Applications in Energy Sciences and Quantum Materials. *Rev. Sci. Instrum.* **2017**, *88*, 013110.
(63) Lu, Y.; Höppner, M.; Gunnarsson, O.; Haverkort, M. W. Efficient Real-Frequency Solver for Dynamical Mean-Field Theory. *Phys. Rev. B: Condens. Matter Mater. Phys.* **2014**, *90*, 085102.
(64) Haverkort, M. W.; Sangiovanni, G.; Hansmann, P.; Toschi, A.; Lu, Y.; Macke, S. Bands, Resonances, Edge Singularities and Excitons in Core Level Spectroscopy Investigated within the Dynamical Mean-Field Theory. *Euro. Phys. Lett.* **2014**, *108*, 57004.
(65) Retegan, M. *Crispy*, v0.7.3; 2019.

NOTE ADDED AFTER ISSUE PUBLICATION

This article was initially published with an incorrect copyright statement and was corrected on or around May 5, 2021.

https://doi.org/10.1021/acs.jpclett.0c03476
J. Phys. Chem. Lett. 2021, 12, 724−731